BIOCHEMISTRY
including biophysical chemistry & molecular biology

Article

pubs.acs.org/biochemistry

Unusual Structural Features Revealed by the Solution NMR Structure of the NLRC5 Caspase Recruitment Domain

Petrus G. M. Gutte,[†] Simon Jurt,[‡] Markus G. Grütter,[†,*] and Oliver Zerbe[‡,*]

[†]Institute of Biochemistry, University of Zurich, Winterthurerstrasse 190, CH-8057 Zurich, Switzerland

[‡]Department of Chemistry, University of Zurich, Winterthurerstrasse 190, CH-8057 Zurich, Switzerland

Supporting Information

ABSTRACT: The cytosolic nucleotide-binding domain and leucine-rich repeat-containing receptors (NLRs) are key sensors for bacterial and viral invaders and endogenous stress signals. NLRs contain a varying N-terminal effector domain that regulates the downstream signaling events upon its activation and determines the subclass to which a NLR member belongs. NLRC5 contains an unclassified N-terminal effector domain that has been reported to interact downstream with the tandem caspase recruitment domain (CARD) of retinoic acid-inducible gene I (RIG-I). Here we report the solution structure of the N-terminal effector domain of NLRC5 and *in vitro* interaction experiments with the tandem CARD of RIG-I. The N-terminal effector domain of NLRC5 adopts a six α-helix bundle with a general death fold, though it displays specific structural features that are strikingly different from the CARD. Notably, α-helix 3 is replaced by an ordered loop, and α-helix 1 is devoid of the characteristic interruption. Detailed structural alignments between the N-terminal effector domains of NLRC5 with a representative of each death-fold subfamily showed that NLRC5 fits best to the CARD subfamily and can be called an atypical CARD. Due to the specific structural features, the atypical CARD also displays a different electrostatic surface. Because the shape and charge of the surface is crucial for the establishment of a homotypic CARD−CARD interaction, these specific structural features seem to have a significant effect on the interaction between the atypical CARD of NLRC5 and the tandem RIG-I CARD.

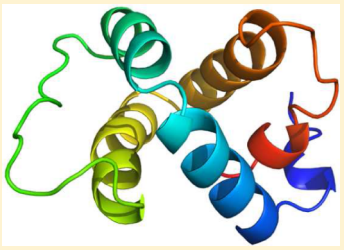

Vertebrates have developed different strategies within the innate and adaptive immune system to defend themselves against a plethora of environmental pathogens. The innate immune system provides the first barrier of defense and contains the class of pattern recognition receptors (PRRs), which are responsible for the detection of pathogens and the following immune response(s). PRRs recognize a pathogen-associated molecular pattern (PAMP) or damage-associated molecular pattern (DAMP) to induce a signaling cascade that results in an inflammatory or antiviral immune response specific for the molecular pattern. The importance of the PRR regulatory activities in the immune system is shown by numerous human autoinflammatory and immune disorders related to impaired activities of PRR family members.[1,2]

PRRs contain four different subfamilies that can be divided into membrane-bound and cytoplasmic receptors.[3] The group of nucleotide-binding domain and leucine-rich repeat containing (NLR) receptors is a subfamily that is active in the cytoplasm and characterized by their tripartite domain architecture. This subfamily contains an N-terminal effector domain, linking the NLR to a downstream signaling cascade; a central nucleotide-binding oligomerization domain (NOD) module responsible for oligomerization, comprising the nucleotide-binding domain (NBD), the helical domain HD1, and the winged-helix domain (WHD);[4] and a C-terminal leucine-rich repeat (LRR), responsible for ligand binding.[5] The NLRs are further divided into subclasses based on their N-terminal effector domain: the NLRA subclass containing an acidic trans-activating domain (AD), the NLRB subclass containing a baculovirus inhibitor repeat domain (BIR), the NLRC subclass with a caspase recruitment domain (CARD), and the NLRP subclass containing a pyrin domain (PYD).[5]

The NLR (sub)family members containing a CARD (NLRC) perform different immune regulatory functions. Upon activation by the protein flagellin, NLRC4 sequentially recruits the adaptor protein ASC and procaspase-1 forming the NLRC4 inflammasome.

This NLRC4 inflammasome activates caspase-1 and finally initiates a pro-inflammatory response by inducing interleukin-1β and interleukin-18 activation.[6] NLRC1 and NLRC2 seem to function without the formation of an inflammasome. When triggered by specific peptidoglycan fragments from the bacterial cell wall, NLRC1 and NLRC2 interact with the receptor-interacting serine/threonine-protein kinase (RIPK) 2 through a homotypic CARD−CARD interaction.[7] RIPK2 triggers the canonical NF-κB and MAPK pathways to initiate several responses, such as the production of pro-inflammatory cytokines.[8,9] NLRC3 has been implicated to modulate the TNF receptor associated factor 6 (TRAF6) activity under noninflammatory conditions.[10] In contrast to other NLRC members, NLRC5 seems to execute two different functions: as a transactivator of MHC class I transcription in immune

Received: February 8, 2014
Revised: April 30, 2014
Published: May 1, 2014

   dx.doi.org/10.1021/bi500177x | *Biochemistry* 2014, 53, 3106−3117

cells[11,12] and as a regulator of immune responses triggered by specific PAMPs.[13,14]

As a transactivator, NLRC5 interacts with transcription factors bound to a conserved W/SXY motif at the promoter region of MHC class I to form a multiprotein complex, upon stimulation with interferon-γ (IFN-γ). This multiprotein complex is called the NLRC5 enhanceosome and induces MHC class I expression.[11,12,15]

As a regulator of innate immune responses, NLRC5 has been linked to NLRP3[14] and RIG-I/MDA5.[13] However, this role remains controversial or unclear as contradictory results have been reported. In transfected human monocytes, stimulated with specific PAMPs and DAMPs, it was shown that NLRC5 is required for NLRP3 inflammasome activation and that it interacts with NLRP3 and the apoptotic speck protein (ASC).[14] However, this result was not supported by overexpression experiments in macrophages in which NLRC5 was shown to be dispensable for a NLRP3 inflammasome response.[16] Others reported NLRC5 to be a negative regulator of an antiviral response and type I interferon production.[13] As a negative regulator, NLRC5 binds IKKα/IKKβ and inhibits their activation and thus the antiviral response.

In mouse macrophages, NLRC5 interacts with the N-terminal tandem CARD of retinoic acid-inducible gene I (RIG-I) and blocks its binding to mitochondrial antiviral signaling protein (MAVS), therefore inhibiting IFN-β signaling.[13]

NLRC5 contains a domain architecture that is characteristic for NLR proteins. In immune signaling the N-terminal effector domain generally determines which signaling cascade is triggered through a homotypic interaction with its ligand. Sequence alignments show that the N-terminal effector domain of NLRC5 is different from other death-fold domains. For that reason the N-terminal effector domain of NLRC5 has been named an atypical death domain or a CARD.[17,18] The CARD family of proteins belongs to the death-fold superfamily, which includes the aforementioned PYD, the death domain (DD), and the death effector domain (DED) family.[19] These domains all arrange in an antiparallel α-helical bundle displaying a Greek key topology.

Because of the particular sequence properties and difficulties to classify the NLRC5 N-terminal effector domain, we decided to determine its three-dimensional structure. Since the role of NLRC5 in immune regulation is still unclear, this structure, together with biochemical interaction experiments, might help in finding its cellular binding partner(s) in immune regulation and in innate immune responses. We describe the structure and backbone dynamics of the mouse NLRC5 N-terminal effector domain. The effector domain possesses a fold similar to the one of the death-fold domains; however, it displays significant differences in the number of core α-helices and their relative orientation. We show here that the N-terminal effector domain of NLRC5 fits best to the CARD subfamily and is therefore called an atypical CARD. We also present *in vitro* binding experiments to test a previously published interaction between the tandem CARD of RIG-I and NLRC5.[13]

MATERIALS AND METHODS

Cloning and Expression. Mouse NLRC5 atypical CARD coding for residues 1 to 96 and residues 1 to 147 was amplified with standard PCR methods and subsequently cloned into the pGEX-6p1 vector (GE Healthcare) using the *Bam*HI (5′) and *Xho*I (3′) restriction sites. As a result, a glutathione S-transferase (GST) tag, together with a human rhinovirus 3C protease (GE healthcare) cleavage site was added to the N-terminus of the mouse NLRC5 atypical CARD. All molecular cloning was performed with standard PCR methods. Transformed *Escherichia coli* Bl21(DE3) cells were grown in M9 minimal medium supplemented with either $^{15}NH_4Cl$ (Sigma-Aldrich) or $^{15}NH_4Cl$ and $^{13}C_6$ D-glucose (Sigma-Aldrich) as the sole sources of nitrogen and carbon for the ^{15}N-labeled and the ^{15}N ^{13}C-labeled mouse NLRC5 atypical CARD, respectively. Overexpression was induced at OD_{600} between 0.6−0.8 with 0.5 mM isopropyl-D-thiol galactosidase (IPTG, Biosolve) and continued for 13−16 h at 30 °C.

Mouse RIG-I tandem CARD (residues 1 to 186) was cloned into a modified pBAD24 expression vector with FX cloning,[20] adding a human rhinovirus 3C protease (GE healthcare) cleavage site, an eGFP-tag, and a decahistidine affinity tag to the C-terminus. Transformed *Escherichia coli* MC1061 cells were grown in LB medium at 37 °C until an OD_{600} between 0.6−0.8 was reached. The expression of the RIG-I 1−186 fusion protein was induced with 2×10^{-2}% of L-arabinose (Sigma-Aldrich) and continued for 16−19 h at 18 °C.

Protein Purification. *Escherichia coli* Bl21(DE3) cells containing the overexpressed mouse atypical CARD of NLRC5 (1−96 and 1−147) were resuspended in lysis buffer (50 mM sodium phosphate, pH 7.3, 100 mM NaCl, 50 mM KCl, 1 mM EDTA, 0.5 mM tris(2-carboxyethyl)phosphine (TCEP, Acros) and Complete Protease Inhibitor (Roche)) and subsequently lysed using the Emulsiflex C3 (Avestin). The cell lysate was centrifuged at 13000 rpm for 45 min at 4 °C, filtered (0.45 μm), and applied to an equilibrated 5 mL Protino GST/4B column (Macherey Nagel). The Protino GST/4B column was subsequently washed with 20 column volumes of lysis buffer. To remove the GST-tag, human rhinovirus 3C protease (GE Healthcare) was diluted to a molecular ratio of 1:20 and applied to the Protino GST/4B column. The column was incubated overnight (13−16 h) at 4 °C. A pre-equilibrated 1 mL GST FF column (GE Healthcare) was attached to the elution end of the Protino GST/4B, and the mouse NLRC5 atypical CARD alone was eluted by applying five column volumes of lysis buffer. The eluted atypical CARD of mouse NLRC5 comprising residues 1 to 96 was further purified to homogeneity in 20 mM 2-(*N*-morpholino)ethanesulfonic acid (Mes), pH 6.2, 100 mM NaCl, 50 mM KCl, and 2 mM TCEP by size-exclusion chromatography using a Superdex S75 10/300 GL (GE Healthcare).

The eluted NLRC5 comprising residues 1−147 was first subjected to overnight dialysis at 4 °C with the ion exchange buffer (50 mM Tris, pH 9, 10% glycerol) before it was applied to a 5 mL ResourceQ column anion exchanger (GE healthcare) and purified with a NaCl gradient. The eluted atypical CARD of mouse NLRC5 comprising residues 1−147 was further purified to homogeneity in 20 mM sodium phosphate, pH 7.5, 60 mM NaCl, and 40 mM KCl by size-exclusion chromatography using a Superdex S75 10/300 (GE Healthcare). Both proteins were concentrated to approximately 0.6 mM for NMR experiments.

MC1061 cells containing the overexpressed tandem CARD of mouse RIG-I were resuspended in lysis buffer (50 mM sodium phosphate, pH 8, 300 mM NaCl, 10 mM imidazole, and Complete Protease Inhibitor EDTA free (Roche)) and subsequently lysed using the Emulsiflex C3 (Avestin). The cell lysate was centrifuged at 13000 rpm for 45 min at 4 °C, filtered (0.45 μm), and applied to equilibrated Protino Ni-NTA agarose (Macherey Nagel). The Protino Ni-NTA agarose was

dx.doi.org/10.1021/bi500177x | *Biochemistry* 2014, 53, 3106−3117

subsequently washed with 100 column volumes of lysis buffer before the protein was eluted in elution buffer (20 mM sodium phosphate, pH 8, 300 mM NaCl, 300 mM imidazole). The eGFP and decahistidine affinity tag were removed by adding human rhinovirus 3C protease (GE Healthcare) to a molecular ratio of 1:20 to mouse RIG-I tandem CARD. Cleavage was performed in a dialysis membrane (MWCO 12−14 kDa, Spectrumlabs), and the products were dialyzed overnight (13−16 h) at 4 °C against the size exclusion chromatography buffer (10 mM 4-(2-hydroxyethyl)-1-piperazineethanesulfonic acid (Hepes), pH 7.4, 150 mM NaCl, 0.5 mM TCEP). After cleavage, the fusion tags were removed by incubating the mixture with equilibrated Protino Ni-NTA agarose. The mouse RIG-I tandem CARD was further purified to homogeneity in size-exclusion chromatography buffer using a Superdex S75 10/300 (GE Healthcare).

NMR Spectroscopy. Human NLRC5 constructs 1−103, 1−111, and 1−133 and mouse NLRC5 constructs 1−96 and 1−130 were all subjected to crystallization trials, but none resulted in crystals. For that reason, we used NMR spectroscopy to determine the structure. [^{15}N,^{1}H]-heteronuclear single-quantum correlation (HSQC) spectra of mouse NLRC5 constructs encoding residues 1−96 and 1−147 were initially compared to select for the most suitable construct. While only a subset of all expected peaks was observed in the longer construct, most of the expected amide moieties were present in the 1−96 construct.

CD spectra revealed typical features of an α-helical protein, with a melting temperature around 66 °C (Figure S1, Supporting Information). Accordingly, all NMR spectra for structural experiments were recorded at 310 K; the NMR perturbation shift assays were recorded at 300 K using Bruker Avance 600 and 700 MHz spectrometers equipped with cryogenically cooled triple-resonance probe heads. Spectra were processed with linear prediction in indirect frequency dimensions, generally applying cosine-bell window functions in the Bruker spectrometer software TOPSPIN 2.3 and transferred into the program CARA[21] for further analysis. Proton chemical shifts were calibrated from the positions of the water line at 4.63 ppm at 310 K, from which the carbon and nitrogen scales were derived indirectly. All NMR experiments were taken from the Bruker pulse program library, and incorporated, whenever possible, the Kay−Rance sensitivity enhancement schemes and coherence selections using pulsed-field gradients. Sequence-specific resonance assignments were accomplished using established procedures. Initially, spin systems were picked in the [^{15}N,^{1}H]-HSQC spectrum. For the sequential backbone assignment, a series of triple resonance spectra were acquired on the uniformly [^{15}N,^{13}C]-labeled atypical CARD of NLRC5 in 95% H_2O/5% $^{2}H_2O$. To link sequential amide moieties, CBCA(CO)NH[22] and HNCACB[23] spectra were recorded to match Cα/Cβ pairs. Carbonyl frequencies were linked using the recorded HNCO[24] and HN(CA)CO.[25] The side chains were assigned using HC(C)H-total correlation spectroscopy (TOCSY)/(H)CCH-TOCSY experiments,[26,27] starting from the assigned Cα/Cβ pairs. The proton frequencies within the aromatic spin systems were annotated using a [^{13}C,^{1}H]-HSQC and ^{13}C-resolved nuclear Overhauser effect spectroscopy (NOESY) centered on aromatic carbons. The aromatic spin systems were linked to the aliphatic side chains using CB(CGCD)HD spectra[28] and aromatic spin systems were annotated with the help of a ^{1}H-TOCSY-relayed ct-[^{13}C,^{1}H]-HMQC experiment.[29] Backbone and side-chain assignment was performed with the software CARA.[21] In addition, torsion-angle restraints were derived from the backbone chemical shifts using TALOS.[30]

With the help of the ATNOS/CANDID protocol,[31,32] UNIO'10 software automatically picked and assigned the ^{15}N- and ^{13}C-resolved NOESY signals.

The peak lists were then automatically annotated by the AUTOASSIGN macro of CYANA 3.0[33] and converted into upper-distance restraints. A total of 1278 upper-distance restraints were used to calculate the final structure using restrained torsion angle molecular dynamics as implemented in the program CYANA 3.0.[33] The CYANA target function in the final run was 1.5. The resulting coordinates for the structure of the atypical CARD of mouse NLRC5 were energy minimized in explicit water using the CHARMM force-field.[34] Of the initially 100 calculated structures, the 20 conformers with the lowest target function were used for energy minimization in CHARMM[34] and for further structural analysis. PyMOL (http://www.pymol.org) was used to analyze the final 20 conformers and to create the figures presenting the molecular models. ^{15}N-relaxation data were recorded using 600 and 150 μM samples on a 700 MHz spectrometer at 310 K with proton-detected versions of the ^{15}N{^{1}H}-steady-state NOE experiment,[35] the Carr−Purcell−Meiboom−Gill (R_2),[36] and the inversion−recovery (R_1)[37] experiments. Relaxation dispersion was measured with the relaxation-compensated CPMG dispersion experiment[38] using eight different CPMG field strengths ranging from 31 to 455 Hz. Peak volumes were integrated within the program SPSCAN that uses line shape deconvolution of signals for proper integration of partially overlapping peaks and evaluated using home-written routines for least-squares fitting. The relaxation data were analyzed in a model-free approach[39,40] using the software DYNAMICS.[41−43] ROTDIF[44] was used to calculate the overall correlation time from the relaxation data. This value was subsequently used in the *Modelfree* analysis. The analysis revealed that a monomer−dimer equilibrium had to be assumed to fit the data. Different values of the dissociation constant K_d in the range between 10 and 900 μM were used resulting in different optimal correlation times τ_c.

Protein Data Bank (PDB) and Biological Magnetic Resonance Bank entry (BMRB). Assigned chemical shifts and coordinates were deposited in the PDB and BMRB databases under accesion codes 2MJM and 19732, respectivly.

Chemical Shift Perturbation Assays. Possible interactions between the atypical CARD of mouse NLRC5 and the tandem CARD of mouse RIG-I were probed by NMR using chemical shift perturbation assays.[45] Therein, spectra recorded on 70 μM solutions of ^{15}N-NLRC5 were measured in the absence and presence of 140 μM of mouse RIG-I tandem CARD at 300 K. These measurements were performed at either pH 6.2 (in 20 mM Mes, 100 mM NaCl, 50 mM KCl, and 2 mM TCEP) or at pH 7.4 (in 10 mM Hepes, 150 mM NaCl, and 2 mM TCEP).

Plasmid Construction and Transient Expression in HEK293T Cells. NLRC5 and RIG-I constructs were cloned into a pcDNA5/FRT-vector (Invitrogen) modified for FX-cloning[20] and supplemented with a sequence encoding for C-terminal affinity tags, adding a Myc-tag (NLRC5) or a C-terminal FLAG-tag (RIG-I) to the C-terminus. As an exception, full-length human NLRC5 was cloned into a pcDNA3 adding a C-terminal SBP-Myc-tag or an eGFP-SBP-Myc-tag. NLRC5 and RIG-I plasmid constructs included mouse NLRC5,

encoding residues 1−96 and 1−130 and denoted as mu96 and mu130, respectively; human NLRC5, encoding residues 1−96, 1−130, 1−550, and 1−1866 denoted as hu96, hu130, hu550, hu1866, and hu1866-eGFP, respectively; mouse RIG-I, encoding residues 1−186, marked as muRIG-I 186; and human RIG-I, encoding residues 1−186 and 1−925, marked as huRIG-I 186 and huRIG-I 925, respectively. All molecular cloning was performed with standard PCR methods in combination with FX cloning.[20]

HEK293T cells were cultured in Dulbecco's modified Eagle's medium (DMEM: Sigma-Aldrich) supplemented with 10% v/v fetal bovine serum (FBS; Sigma-Aldrich) and 1% penicillin/streptomycin (Sigma-Aldrich). The cells were maintained at 5% (v/v) CO_2 at 37 °C. Expression plasmids were separately transfected in HEK293T cells using polyethylenimine (PEI, Sigma-Aldrich).[46]

Co-immunoprecipitation Assays. For cell lysis, HEK293T cells were isolated from the culture medium by centrifugation (300*g*, 3 min, at room temperature), resuspended in lysis buffer (50 mM Tris, pH 7.5, 150 mM NaCl, 1% Nonidet P-40 substitute (Fluka), and EDTA-free Complete Protease Inhibitor (Roche)), and incubated on ice for 30 min. Subsequently, the cell extract was centrifuged at 13000 rpm for 30 min at 4 °C, followed by the isolation of the cell lysate from the cell pellet. The cell lysates containing a Myc-tagged protein were subjected to a precleaning step to remove proteins that bind unspecifically to the M2-affinity gel (Sigma-Aldrich). The cell lysate was added to 30 μL of sepharose 6B (Sigma-Aldrich), which was pre-equilibrated in lysis buffer, and incubated at 4 °C for 30 min with light agitation, and followed by the isolation by centrifugation (1000*g*, 5 min, at 4 °C). The cell lysates containing FLAG-tagged protein were added to 25 μL of M2-affinity gel (Sigma-Aldrich) that was equilibrated in lysis buffer, followed by three rounds of washing with lysis buffer to remove unbound proteins. The precleaned cell lysates that contained the Myc-tagged protein were then added to the FLAG-tagged proteins that were bound to the M2-affinity gel and incubated for 1 h at 4 °C with light agitation. The M2-affinity gel was centrifuged at 1000*g* for 5 min at 4 °C, and the supernatant was removed before the M2-affinity gel was subjected to 4 rounds of washing with the lysis buffer. The FLAG-tagged proteins were subsequently eluted from the M2-affinty gel by adding 55 μL of 0.1 M glycine, pH 3.5, for 10 min on ice.

The elution reaction was stopped by adding 10 μL of 1 M Tris, pH 7.5, 1.5 M NaCl. The M2-affinity gel was centrifuged at 1000*g* for 5 min at 4 °C to isolate the supernatant, before it was mixed with 15 μL of SDS-loading buffer and subjected to SDS-PAGE and Western blot analysis.

RESULTS

Cloning, Expression, and Purification. Constructs of the atypical CARD of human NLRC5 encoding for residues 1−103, 1−112, and 1−130 and the atypical CARD of mouse NLRC5 encoding for residues 1−96 and 1−147 all showed high levels of soluble expression. Because the mouse constructs delivered the highest yield of soluble protein, we decided to focus on the atypical CARD of mouse NLRC5 comprising residues 1−96 and 1−147 for the structure determination with solution NMR. Mouse NLRC5 (1−96) was purified to homogeneity at pH 6.2 (Figure S2, Supporting Information). The protein was stable for weeks after purification; however, signs of oligomerization were detected over this period at 37 °C, room temperature, and 4 °C. Addition of 2 mM of the reducing agent TCEP to the purification buffers prevented oligomerization, suggesting that oligomerization was induced by oxidation of surface-exposed cysteine residues through disulfide bond formation.

Structure Determination of the Atypical CARD of NLRC5. Based on [^{15}N,^{1}H]-HSQC spectra, the mouse NLRC5 construct encoding residues 1−96 was selected for three-dimensional structure determination. While only a subset of all expected peaks was observed in the construct encoding for mouse NLRC5 residues 1−147 (data not shown), almost all expected amide moieties were present in the mouse NLRC5 residues 1−96 construct.

Backbone and side-chain assignments for the atypical CARD of mouse NLRC5 could be completed to 94%. The missing assignments included residues Asn14, Asn15, Val86, Asp89, and Met90 (Figure S3, Supporting Information). The five amino acid remnant at the N-terminus that originates from the 3C cleavage site (GPLGS) was not included in the structure determination and further structural analysis.

The NMR Structure of the Atypical CARD of Mouse NLRC5. The structure of the atypical CARD of mouse NLRC5 consists of five defined α-helices (α1, 2, 4, 5, and 6) that are closely packed around a hydrophobic core. A sixth α-helix (α0) does not contribute to the hydrophobic core and a loop instead of an expected α-helix connects helices α2 and α4 in the core (Table 1, Figure 1A,B). The α-helices encompassing residues 9−12 (α0), 16−28 (α1), 30−40 (α2), 55−68 (α4), 70−84 (α5), and 91−95 (α6), all are arranged in an antiparallel fashion, and five are stabilized around a hydrophobic core, a feature that is common in death-fold domains. As shown in Figure 1C, the residues that form the hydrophobic core are Leu22 and Leu26 in α-helix 1, Leu33 and Leu37 in α-helix 2, Ile58, Leu62, and Leu65 in α-helix 4, and Trp73, Phe76, Ile77, Leu80, and Leu84 in α-helix 5. Supporting the hydrophobic core are Trp19 (α1), Trp32 (α2), Phe40 (α4), and Leu94 (α6). In addition, Ile97 at the C-terminus has direct contact to the hydrophobic core. α-Helix 0 does not contribute to the hydrophobic core since it points away from the center and is positioned on the outer surface of α-helix 6. This orientation is fixed by a salt bridge between Asp7 and Lys74 (data not

Table 1. Structural Statistics for the 20 Lowest Energy Structures

NMR Distance Restraints (All)	
total NOE	1278 (100%)
intraresidue ($\|i-j\|=0$)	429 (33.6%)
sequential ($\|i-j\|=1$)	347 (27.2%)
short-range ($\|i-j\|\leq 1$)	776 (60.7%)
medium-range ($1<\|i-j\|<5$)	304 (23.8%)
long-range ($\|i-j\|\geq 5$)	198 (15.5%)
Deviations from Idealized Geometry	
bond lengths (Å)	0.016
bond angles (deg)	1.4
Ramachandran Plot Statistics (6−98; NMR-PROCHECK)	
residues in most favored regions (%)	86.4
residues in additionally allowed regions (%)	11.4
residues in generally allowed regions (%)	1.1
residues in disallowed regions (%)	1.1
Pairwise rmsd (Å)	
backbone (N, Cα, C, O)	0.59 ± 0.10
all heavy atoms	1.72 ± 0.4

dx.doi.org/10.1021/bi500177x | *Biochemistry* 2014, 53, 3106−3117

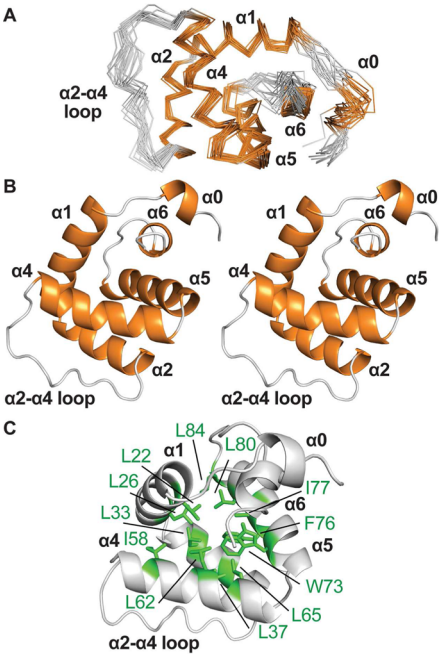

Figure 1. The solution structure of the atypical CARD of mouse NLRC5. (A) Ensemble of the 20 lowest-energy structures showing residues 6−98 in which the α-helices are highlighted in orange, the loops in gray. (B) Cartoon representation of the lowest-energy conformer of the atypical CARD of mouse NLRC5 presented in stereoview. (C) The conserved central hydrophobic core of the atypical CARD of mouse NLRC5. The side-chains are shown in sticks and highlighted in green.

shown). α-Helices 1−2 and 4−5 are connected by short well-defined loops. In contrast, α-helix 1 and 6 are preceded by loops that are 3 and 6 amino acids long, respectively. These two loops contain amino acids for which no resonances were observed in the [^{15}N,^{1}H]-HSQC spectrum (Asn14, Asn15, Asp89, Met90), indicating the presence of conformational or chemical exchange.

The most striking feature of the atypical CARD of mouse NLRC5 is the long loop comprising residues 41−54 that connects α-helix 2 and α-helix 4, from hereon called α2−α4 loop (Figure 1A,B).

Based on the 20 most energetically favorable structures this α2−α4 loop is ordered but displays a higher flexibility than the helical segments contributing to the core structure. Indeed, comparison of the loop sequence with other helical sequences in the atypical CARD of mouse NLRC5 and death-fold domains revealed that it has a lower helical propensity (data not shown).

Interestingly, the α2−α4 loop is only stabilized by a small number of hydrophobic residues, mainly at the start of the loop (Figure S4, Supporting Information). Leu41, the first residue of the loop, is in a hydrophobic contact with Leu37 (α2), Leu40, and Leu65 (α5). The hydrophobic interaction between Tyr50 and Val57 (α5) stabilizes the C-terminal part of the loop. The center of the α2−α4 loop seems not to be stabilized by any hydrophobic interactions because the hydrophobic side chains of Leu46 and Met44 are directed outward and away from α-helices 2 and 4. Mouse and human NLRC5 atypical CARD share a sequence identity and similarity of 50% and 62%, respectivly. The nonsimilar residues are spread out over the entire sequence and are mainly present in the helices. A sequence comparison for the α2−α4 loop reveals less hydrophilic (2 versus 5) and more hydrophobic residues (3 versus 1) in the mouse ortholog in comparison to the human ortholog.

Structural Comparison with the Death-Fold Superfamily. The structures most similar to the atypical CARD of mouse NLRC5 as identified by the DALI-server[47] are those of CARDs, as shown in Table 2.

Table 2. Superposition of the Atypical CARD of Mouse NLRC5 and Death-Fold Domains

protein	domain	PDB id	Z score[a]	rmsd (Å)[a]	aligned Cα[b]
ICEBERG	CARD	1DGN	6.6	2.7	74
NOD1	CARD	4E9M	6.5	2.5	68
DARK	CARD	1VT4	6.0	2.8	80
Apaf-1	CARD	1C15	5.7	3.2	77
Fas	DD	3EZQ	5.7	4.3	74
UNC5H2	DD	1WMG	5.7	2.3	68
NLRP3	PYD	3QF2	3.4	3.4	72
NLRP7	PYD	2KM6	4.2	2.9	73

[a]The rmsd and Z scores were calculated using the DALI server.[47] [b]The aligned Cα depicts the amount of residues that could be aligned for this particular structural alignment. The list is ordered by decreasing Z scores.

These Z-score matches are lower than generally observed within a death-fold subfamily (e.g., CARMA1 CARD/Apaf-1 CARD, Z-score 14.4; Apaf-1 CARD/ICEBERG CARD, Z-score 11.1; NLRP3 PYD/ASC PYD, Z-score 13.8). In addition, the atypical CARD of mouse NLRC5 is related to the other death-fold subfamilies with similar DALI-server statistics (Table 2). This comparison shows that the atypical CARD of mouse NLRC5 has structural features that are common to all four subfamilies, features that are only similar to the CARD, DD, and PYD subfamily, and features that are clearly different from any of the four subfamily folds.

In order to classify the atypical CARD of mouse NLRC5 in the death-fold superfamily, we performed a structural alignment with all four subfamilies (DED, DD, CARD, and PYD) using the secondary structure matching (SSM) algorithm[48] (Figure 2).

Because the spatial arrangement of the N- and C-termini of the death-fold domains within their subfamilies is very different in comparison to the core, we focused on the spatial arrangement of α-helices 2, 3, 4, and 5 of the death-fold domains to initially classify the atypical CARD of mouse NLRC5 into one of the four death-fold subfamilies, supported by the specific structural features of every death-fold subfamily.[49−52]

The structural alignments indeed revealed that the spatial arrangement of α-helices 2, 4, and 5 (and the α2−α4 loop) of the atypical CARD of mouse NLRC5 is very similar to that of all death-fold domain structures, with only small differences in the relative tilt angles. This notion is supported by the fact that a large portion of the amino acids involved in the formation of the hydrophobic core in the death-fold domains are conserved in α-helices 2, 4, and 5 of the atypical CARD of mouse NLRC5 (Figure 2A). The most striking difference in the atypical CARD of mouse NLRC5 in comparison to the death-fold domains is the absence of α-helix 3. The PYD subfamily is an exception, because the absence of α-helix 3 is a structural characteristic that is known from the NLRP1 PYD and that is very similar to

dx.doi.org/10.1021/bi500177x | Biochemistry 2014, 53, 3106−3117

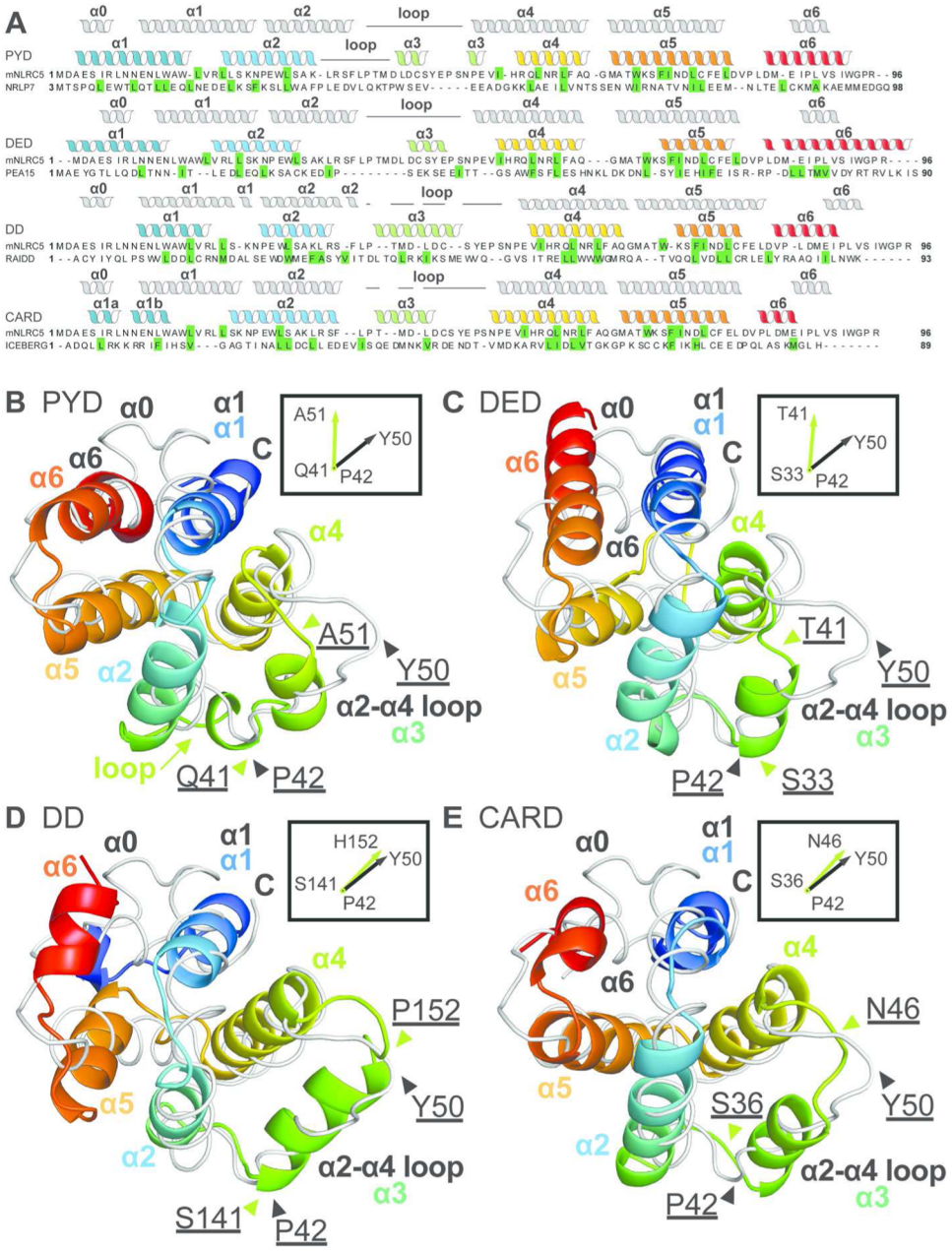

Figure 2. Structural comparison of the atypical CARD of mouse NLRC5 with representatives of the four death-fold subfamilies. The atypical CARD of mouse NLRC5 is shown in a gray ribbon presentation. The representatives of the death-fold subfamilies are presented in cartoon and in spectrum color. The pairwise rmsd between the atypical CARD of NLRC5 and all other death-fold domains was calculated by superposition of Cα atoms of α-helices 0/1−6. The orientation of the α2−α4 loop axis (black arrow) is depicted schematically in relation to the axis orientation of α-helix 3 (green arrow) of the overlaid death-fold domain. The residues in the figure and the schematic drawing indicate the boundaries, which were taken for the axis orientation of the α2−α4 loop axis (black) and the overlaid death-fold domain (green). (A) Sequence representation of the structural alignments. Residues that constitute the hydrophobic core are labeled in green. (B) Structural alignment of mouse NLRC5 atypical CARD with the PYD of NLRP7 (PDB 2KM6; rmsd 3.020 Å). (C) Structural alignment of mouse NLRC5 atypical CARD with the DED of PEA-15 (PDB 1N3K; rmsd 3.081 Å). (D) Structural alignment of NLRC5 atypical CARD with the DD of RAIDD (PDB 3MOP; rmsd 3.314 Å). (E) Structural alignment of NLRC5 atypical CARD with the CARD of ICEBERG (PDB 1DNG; rmsd 2.165 Å).

the loop region connecting α-helix 2 and 3 in all other PYD structures (Figure 2B).[53]

However, the α2−α4 loop of the atypical CARD of mouse NLRC5 and that of the PYDs are different in length (e.g., 18 amino acids in NLRP1 PYD versus 13 amino acids in the atypical CARD of mouse NLRC5), as is the orientation relative to α-helices 2 and 4. As shown for NLRP7 PYD, α-helix 3 has a very different orientation in comparison to the α2−α4 loop of the atypical CARD of mouse NLRC5 (Figure 2B). In addition, α-helix 4 in the PYD fold is shorter than in the atypical CARD of mouse NLRC5.

In the comparison to the DED of PEA-15, α-helix 3 of the DED-fold shows similarities to α-helix 3 of NLRP7 PYD and hence a very different orientation in comparison to the α2−α4 loop of the atypical CARD of mouse NLRC5 (Figure 2C). In addition, the DED subfamily is characterized by the presence of a RxDL-motif that is absent in the atypical CARD of mouse NLRC5.[19]

dx.doi.org/10.1021/bi500177x | *Biochemistry* 2014, 53, 3106−3117

The $\alpha2-\alpha4$ loop of the atypical CARD of mouse NLRC5 has a very similar direction as α-helix 3 of the RAIDD DD (Figure 2D).[19] However, α-helices 2 and 5 of the DD-fold do not align well with the α-helices 2 and 5 of the atypical CARD of mouse NLRC5, in contrast to the other death-fold domains.

To summarize, based on the structural alignment of α-helices 2, 4, 5, and α-helix 3/loop $\alpha2-\alpha4$, the atypical CARD of mouse NLRC5 displays the best fit with the CARD-fold (Figure 2E). In the following, we provide a more detailed analysis of the CARD features. Besides the $\alpha2-\alpha4$ loop, the most dramatic difference between the atypical CARD of mouse NLRC5 and the general CARD-fold is the absence of the characteristic interruption in the first α-helix (Figure 2E and Figure 3A). As a result, α-helix 1a and 1b are directly joined in the atypical CARD of mouse NLRC5 into one helix ($\alpha1$) that displays a similar orientation as helix 1b of the ICEBERG CARD. The atypical CARD of mouse NLRC5 contains an additional short helical segment preceding α-helix 1 (Figure 3A).

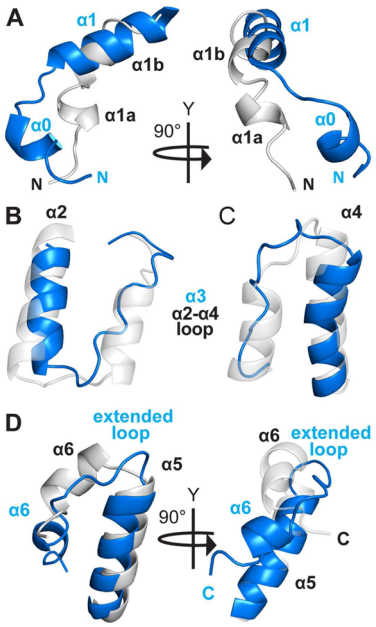

Figure 3. Detailed structural comparison of the atypical CARD of mouse NLRC5 with ICEBERG-CARD. Cartoon presentation of the atypical CARD of mouse NLRC5 (blue) and ICEBERG (gray). (A) NLRC5 atypical CARD α-helix 0 and 1 overlaid with the interrupted first α-helix (1a, 1b) of ICEBERG CARD. (B) NLRC5 atypical CARD α-helix 2 and loop $\alpha2-\alpha4$ overlaid with α-helix 2 and α-helix 3 of ICEBERG CARD. (C) NLRC5 atypical CARD loop $\alpha2-\alpha4$ and α-helix 4 overlaid with α-helix 3 and 4 of ICEBERG CARD. (D) The atypical CARD of NLRC5 α-helix 5 and 6 overlaid with the α-helix 5 and 6 of ICEBERG CARD.

The ICEBERG CARD contains an α-helix 3 that has a very similar orientation as the $\alpha2-\alpha4$ loop, while maintaining the strong alignment with α-helix 2 and 5 of the atypical CARD of mouse NLRC5 (Figure 3B,C). In addition, α-helix 4 of both domains has the same length and, with the exception of a small tilt in the N-terminal domain of NLRC5, aligns well. At the C-terminus of the CARD structures, α-helix 6 displays some variability in its orientation and length and a characteristic short loop that connects α-helix 5 to α-helix 6. However, in the atypical CARD of mouse NLRC5, the short α-helix 6 is directed away from α-helix 5 due to an extended six amino acid long loop (Figure 3D).

Based on these structural alignments, the atypical CARD of mouse NLRC5 resembles most but not all characteristics of the CARD subfamily. Therefore, the N-terminal effector domain of mouse NLRC5 can indeed be called an atypical CARD.

Backbone Dynamics Probed via ^{15}N Relaxation. To probe for internal backbone dynamics via ^{15}N relaxation, we measured ^{15}N T1, T2, and ^{15}N{^{1}H}-NOE relaxation data at concentrations of 600 and 150 μM (Figure 4). The ^{15}N{^{1}H}-NOE relaxation data unambiguously demonstrate that most parts of the protein display a defined structure (Figure 4A).

Furthermore, the ^{15}N{^{1}H}-NOE continuously increases from residues 1 to 17, indicating that the N-terminus is flexible. Moreover, the NOE drops for residues 40–57, reflecting the increased flexibility of the $\alpha2-\alpha4$ loop. Residues of all other loops do not display increased flexibility. Interestingly, the increased flexibility of the $\alpha2-\alpha4$ loop is picked up by the R2 but not by the R1 values (Figure 4B,C). In addition, no long-range NOEs to protons in the others part of the domain were observed for the $\alpha2-\alpha4$ loop (Figure S5, Supporting Information).

We noticed, however, strongly increased values of R2 for residues localized on the surface formed by α-helices 1 and 6 and the loop connecting α-helices 5 and 6 due to contributions from exchange to the transverse relaxation rate (Figure 4C,E). Unfortunately, signals for residues 1–15 were broadened so much in the 150 μM sample that we could not analyze data for those residues. Interestingly, the residues corresponding to increased R2 values form a large hydrophobic patch on the surface of the protein, suggesting that this surface patch acts as a dimerization interface (Figure 5A). Using a model-free approach, we calculated a correlation time (τ_c) of 7.49 ns (600 MHz data) to 7.55 ns (700 MHz data) from the relaxation data of residues 21–39 and 57–79 for the data recorded at a concentration of 600 μM. This value is larger than expected for a polypeptide of 96 residues,[54] indicating that a transient formation of dimers is likely to occur at the 600 μM concentration used for the ^{15}N relaxation experiments. A similar increase in overall correlation time was recently observed for the second CARD of human RIG-I.[55] We noticed that better fits resulted and that less parameters were required when data were fitted to a dimer model. With the ^{15}N{^{1}H}-NOE, R1 and R2 data recorded at both 600 (Figure S6, Supporting Information) and 700 MHz best results were obtained when a dissociation constant of 100 μM and an overall correlation time of 4.0 ns for the monomer was used.

A larger number of residues for which model 3, which requires S^2, R_{ex}, and τ_{loc}, is needed in the monomer case can be fit with model 2 (S^2 and R_{ex}) in the dimer case. Fewer contributions from slow local motion are required at an increase of exchange-affected residues. Moreover, the number of residues for which no appropriate model can be found is significantly smaller.

In general, reduced values for the order parameter S^2 were observed for residues comprising the $\alpha2-\alpha4$ loop, confirming the increased flexibility within the loop (Figure 4D). In addition, the analysis indicates that several residues are affected by exchange (Figure 4E).

In order to assess whether exchange contributions are due to conformational exchange or due to a monomer–dimer equilibrium, the sample was diluted to a concentration of 150 μM, and all relaxation measurements were repeated (Figure 4A–C, red curves). In general, a decrease in transverse relaxation rates was observed. At that concentration, the fitted

dx.doi.org/10.1021/bi500177x | Biochemistry 2014, 53, 3106–3117

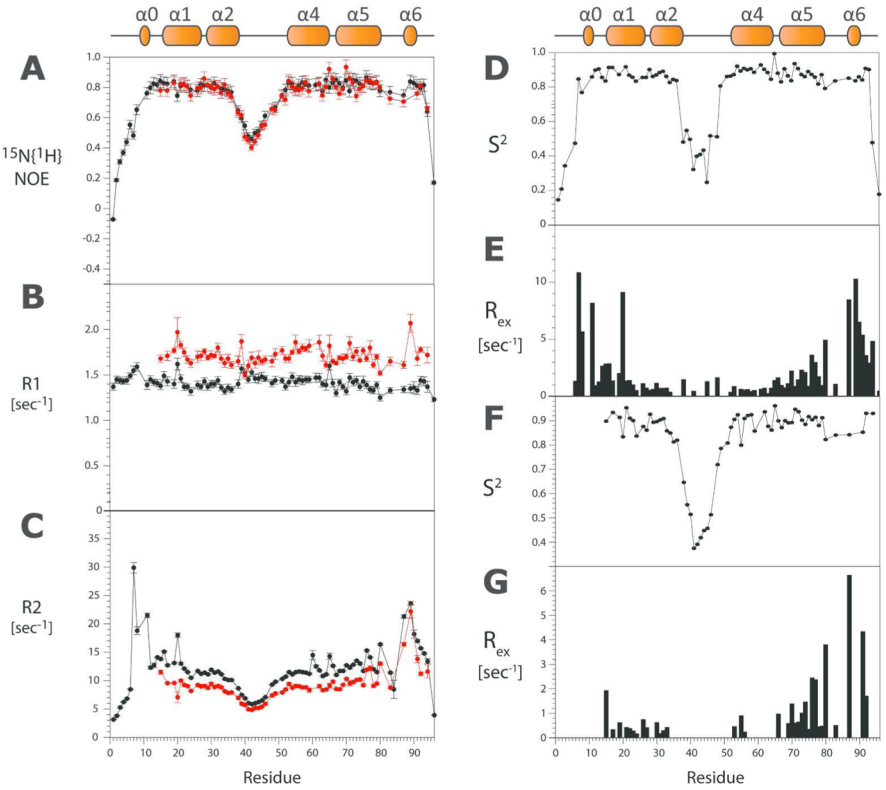

Figure 4. ^{15}N backbone dynamics of the atypical CARD of mouse NLRC5. (A–C) ^{15}N relaxation as measured on a 700 MHz spectrometer at 310 K as observed for the 1–96 construct of the atypical CARD of mouse NLRC5 at concentrations of 600 μM (black circles) and 150 μM (red circles). Experimentally derived secondary structure elements of the atypical CARD of mouse NLRC5 are depicted on top of the figure. (A) ^{15}N{^{1}H}-NOE as well as the (B) R1 and (C) R2 relaxation rates of the atypical NLRC5 CARD. (D–G) Motional parameter derived from a *Modelfree* analysis for data from the 600 μM (D, E) and 150 μM (F, G) samples. Depicted are the generalized order parameter S^2 (D, F) and the exchange contribution Rex (E, G). The *Modelfree* analysis assumed a monomer–dimer equilibrium with a K_d of 100 μM and a global correlation time of 4.0 and 3.8 ns for the 600 μM and the 150 μM sample, respectively.

global correlation time was 5.96 and 5.71 ns for the 600 and 700 MHz data, respectively, still signifiantly higher than the expected approximately 4 ns. Accordingly, the *Modelfree* anaylsis was performed still using the monomer–dimer model (Figure 4F,G). With the exception of the N-terminal 15 residues, slightly smaller exchange contributions were required to model the observed relaxation rates (Figure 4G).

To further investigate these exchange contributions, CPMG relaxation dispersion experiments have been measured. However, relatively poor, featureless dispersion profiles (Figure S7, Supporting Information) with a mostly flat, uniform slope were observed for most of the exchange affected residues, being typical for exchange in the *fast* regime, and an exchange rate that is much larger than the maximum CPMG pulse repetition rate ($k_{ex} \gg \max(\nu_{cpmg})$).

Electrostatic Surface Charges of the NLRC5 Atypical CARD. Probing the surface of the atypical CARD of NLRC5 showed that it has two putative interaction surfaces: the hydrophobic patch formed by α-helices 1 and 6 and the loop connecting α-helix 5 and 6 (Figure 5A) and a negatively charged surface patch comprising Glu31, Asp79, Glu83, and Asp85 (Figure 5B). If we compare this negatively charged surface patch to charged surfaces in other CARDs, it becomes clear that it lacks the distinct concave or convex shape that is responsible for the homotypic (type I and type III) CARD–CARD interactions (data not shown).[56]

In addition, the negatively charged surface patch of the mouse NLRC5 atypical CARD is not located on any of the surface patches that are known to be involved in the homotypic CARD–CARD interactions (type I and type III)[56,57] or the homotypic DD–DD interactions (type I, type II, and type III) (data not shown).[19]

Modeling a second monomer on the hydrophobic surface patch resulted in the model of an atypical mouse NLRC5 CARD dimer, creating a new negatively charged surface patch (residues Glu31, Glu83, and Asp85) as a putative interaction surface (Figure 5C,D).

Coimmunoprecipitation Assays. Cui et al. performed coimmunoprecipitation assays in which they showed that full-length human NLRC5 interacts with full-length human RIG-I and an isolated (tandem) CARD in HEK293T cells, indicating that both proteins interact through a homotypic CARD–CARD interaction.[13] To further characterize this interaction, we created several truncations of both human and mouse isoforms of NLRC5 and RIG-I to conduct interaction assays using protein overexpressed in HEK293T cells.

To probe the interaction between the atypical CARD of NLRC5 and the RIG-I tandem CARD in *in vitro* coimmunoprecipitation assays, we used two constructs of mouse NLRC5 (mu96 and mu130) and six constructs of human NLRC5 (hu96, hu130, hu550, hu1866, and hu1866-eGFP) in combination with either mouse RIG-I (mu186) or human (hu186, hu925) constructs. In contrast to Cui et al.,[13] all constructs were separately expressed in HEK293T cells and combined only after cell lysis for the *in vitro* coimmunoprecipitation assays. In none of these experiments was it possible

dx.doi.org/10.1021/bi500177x | *Biochemistry* 2014, 53, 3106–3117

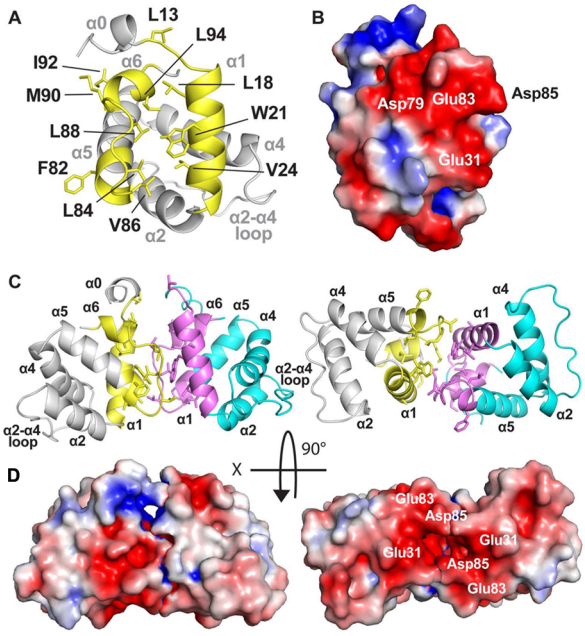

Figure 5. Surface representation of the atypical CARD of mouse NLRC5. (A) Cartoon representation of the atypical CARD of NLRC5 in which the residues that show increased R2 values as measured in the ^{15}N backbone dynamics, and thus indicated to be involved in a putative dimerization interface, are shown in yellow. Residues that are involved in the formation of the putative dimerization of the atypical CARD of mouse NLRC5, as indicated by the increased R2 values in the ^{15}N backbone dynamics, are labeled and depicted as sticks. (B) Electrostatic surface representation of the atypical CARD of mouse NLRC5 rotated 160° over the *Y*-axis and 30° over the *X*-axis in comparison to panel A. A positive surface charge is colored blue, a negative surface charge is colored red, and a neutral surface is colored white. The residues that form the negatively charged patch in the monomeric NLRC5 atypical CARD (Glu31, Asp79, Glu83, and Asp85) are labeled. (C) The dimer of the atypical CARD of NLRC5 in cartoon representation as modeled by the ClusPro 2.0 server.[62] The left presentation of the dimer is rotated 90° over the *Y*-axis in comparison to the monomer in panel A. (D) Electrostatic surface representation of the modeled dimer of the atypical CARD of mouse NLRC5. The residues that form the negatively charged patch of the dimer (Glu31, Glu83, and Asp85) are labeled.

to detect an interaction between RIG-I and the atypical CARDs of mouse and human NLRC5 (Figure S8, Supporting Information).

NMR Chemical Shift Mapping. Alternatively we have probed for NLRC5−RIG-I interactions by chemical shift perturbation (CSP) assays. This assay contains only the two putatively interacting purified proteins, lacking any other cellular components.

^{15}N−^{1}H correlation spectra of 70 μM ^{15}N-labeled atypical CARD of mouse NLRC5 (1−96 AA) in the absence or presence of 140 μM purified mouse RIG-I tandem CARD (Figure S1, Supporting Information) were compared. The measurements at pH 6.2 and pH 7.4 displayed identical peak positions before and after the addition of RIG-I (1−186 AA). This indicated that no direct interaction between the atypical CARD of mouse NLRC5 and the tandem CARD of mouse RIG-I occurs at a biologically relevant strength under these conditions (data not shown).

DISCUSSION

Death-fold domains play a pivotal role in signaling pathways of the immune system and cell death pathways, like apoptosis and necroptosis.[58,59] In the last years, the structures of numerous death-fold domains have been reported. In these studies, it was shown that the different death-fold subfamilies have a very similar topology in which six α-helices bundle around a hydrophobic core in an antiparallel fashion. Therefore, there is a limited set of structural features that differentiate the death-fold domain subfamilies from each other and their specific native ligands.

To provide insight into the immune regulatory function that NLRC5 maintains, we determined the solution structure of the mouse NLRC5 atypical CARD using solution NMR spectroscopy and performed *in vitro* interaction studies between NLRC5 and RIG-I. The structure of the atypical CARD of mouse NLRC5 resembles the overall fold seen in the death-fold superfamily, with the conservation of several of the residues involved in the hydrophobic core. Internal backbone dynamics, specifically the R2-values and the ^{15}N{^{1}H}-NOE, revealed that the atypical CARD of mouse NLRC5 is rigidly folded, except for its flexible N-terminus and the loop connecting α-helix 2 and 4, as well as at the C-terminus. These results clearly show that the atypical CARD of mouse NLRC5 displays distinct differences in comparison to all four death-fold subfamilies. The high sequence similarity suggests that the human ortholog exhibits a structure similar to that of the atypical CARD of mouse NLRC5.

First of all, the atypical CARD of mouse NLRC5 contains a structured loop (α2−α4 loop) that does not participate in the hydrophobic core at the position at which α-helix 3 occurs in the DED, DD, CARD, and PYD folds. This variation is very similar to the PYD fold, except that PYD contains a more flexible loop and a short α-helix 3 that clearly has an orientation different from the α2−α4 loop of the mouse NLRC5 atypical CARD.

In the DED-fold, α-helix 3 is similarly oriented as in the PYD and contains the RxDL-motif, which is absent in the atypical CARD of mouse NLRC5. Except for the α2−α4 loop, both the DD-and CARD-fold possess strong similarities to the atypical CARD of mouse NLRC5. However, when taking the alignment of α-helices 2, 3, and 4 into account, the atypical CARD of mouse NLRC5 is in a better agreement with the CARD-fold.

A more detailed comparison of the atypical CARD of mouse NLRC5 with the ICEBERG CARD, its closest homologue according to the DALI-server, clearly reveals striking differences between both folds such as the noninterrupted α-helix 1, the replacement of α-helix 3 by the α2−α4 loop, the presence of a short α-helix 0 succeeded by a three amino acid long loop, and the fact that α-helix 6 is attached to α-helix 5 by a unusually extended six amino acid long loop. Based on these observations, we decided to classify the N-terminal effector domain of mouse NLRC5 as an atypical CARD.

The homotypic DD−DD interaction can be established with three types of interaction modes (types I, II and III).[19,57] Out of these three possible modes, two have been reported (type I and type III) for the homotypic CARD−CARD interaction.[56,57] From the interaction between the CARDs of Apaf-1/procaspase-9,[56] RAIDD/caspase 2,[49] and NOD1/RICK,[7] it is known that electrostatic interactions between complementary charged and shaped surfaces provide a tight CARD−CARD interaction. The interaction patches involved in these

dx.doi.org/10.1021/bi500177x | *Biochemistry* 2014, 53, 3106−3117

interactions modes are composed of α-helix 1/α-helix4 (patch Ia), α-helix 2/α-helix 3 (patch Ib), α-helix 3 (patch IIIa), and loop α1−α2/loop α3−α4 (patch IIIb).

It is clear that the unique features of the NLRC5 atypical CARD can strongly influence the possible modes of interaction. For instance, it is very likely that the uniquely structured α2−α4 loop is involved in a type III interaction, which possibly triggers structuring and formation of a full α-helix 3.

In addition, α-helix 0 and the uninterrupted α-helix 1 may support a type I interaction as observed for the CARD-fold. The negatively charged surface patch (residues Glu31, Glu83, and Asp85) of the atypical CARD of NLRC5 does not share the shape and location with the interaction epitopes involved in the three homotypic death-fold interaction modes. Therefore, it is clear that the homotypic interaction of NLRC5 atypical CARD with its binding partner RIG-I tandem CARD must be different from the previously described homotypic CARD−CARD interactions.

Exchange contributions to R2 relaxation rates for residues of helices 1 and 6 and the α5−α6 loop, which form an extensive hydrophobic surface patch, indicate that these residues likely act as a dimerization interface. Because NLR proteins are known to oligomerize upon activation, it is possible that full-length NLRC5 exhibits auto-oligomerization activity and the site of interaction with the native ligand may then be part of the thereby formed surface.[60] This hypothesis is supported by the formation of a negatively charged surface patch upon dimerization of the atypical CARD of mouse NLRC5 involving Glu31, Glu83, and Asp85. We like to note here that Glu83 is not conserved in other species.

In contrast to Cui et al., who performed classical coimmunoprecipitation assays in HEK293T cells,[13] our coimmunoprecipitation assays involved the separate expression and the lysis of HEK293T cells *before* combining the putative interaction partners. In this specific experimental setup, using the (mouse and human) atypical CARD of NLRC5 and (mouse and human) RIG-I tandem CARD constructs, we demonstrate that these proteins do not interact. This result was supported by the absence of chemical shift perturbations in the NMR experiments involving the atypical CARD of mouse NLRC5 (1−96) and the tandem CARD of mouse RIG-I tandem (1−186).

Since these proteins interact in the cell, adapter proteins might be required, as for the RIG-I/MAVS interaction,[61] RIG-I lysine K63 ubiquitin ligation is required for interaction.

This approach indicates that the atypical CARD of mouse NLRC5 and the tandem CARD mouse RIG-I might interact through the hydrophobic surface formed by α-helices 1 and 6 and the α5−α6 loop (data not shown).

To analyze the interaction between the atypical CARD of NLRC5 and the tandem CARD of RIG-I, it is important to probe for interactions in cellular systems that allow such modifications and provide possible adapter proteins. For in-depth characterization of biochemically relevant interactions on a molecular level, methods such as yeast two hybrid or tandem mass spectrometry assisted interaction assays using cell extracts might be needed.

■ ASSOCIATED CONTENT

Supporting Information

Results and figures of CD spectroscopy/thermal unfolding, SEC chromatograms, SDS-PAGE analysis, NMR spectra, the hydrophobic contacts in the α2−α4 loop, NOE constraints, ^{15}N relaxation data at 600 MHz, relaxation dispersion profiles, and coimmunoprecipitation results. This material is available free of charge via the Internet at http://pubs.acs.org.

■ AUTHOR INFORMATION

Corresponding Authors

*Prof. M. G. Grütter. Tel: + 41 44 635 5580. Fax: + 41 44 635 6834 E-mail: gruetter@bioc.uzh.ch.

*Prof. O. Zerbe. Tel: + 41 44 635 42 63 Fax: + 41 44 635 6882 E-mail: oliver.zerbe@chem.uzh.ch.

Funding

This work was financially supported by a Swiss National Science Foundation Grant (No. 31-1022181 to M.G.G.).

Notes

The authors declare no competing financial interest.

■ ACKNOWLEDGMENTS

We acknowledge the late Prof. J. Tschopp (University of Lausanne, Switzerland) for providing us with the plasmids containing the NLRC5 and human RIG-I gene. We like to thank Damien Morger for performing the CD experiments and for his input on the analysis.

■ ABBREVIATIONS

AD, acidic transactivating domain; ASC, apoptotic speck protein; BIR, baculovirus inhibitor repeat domain; CARD, caspase recruitment domain; DD, death domain; DED, death effector domain; HD1, helix domain 1; rmsd, root-mean-square deviation; LRR, leucine-rich repeats; MAVS, mitochondrial antiviral signaling protein; NBD, nucleotide binding domain; NLR, nucleotide-binding domain and leucine-rich repeat-containing protein; NMR, nuclear magnetic resonance; NOD, nucleotide oligomerization domain; PAMP, pathogen associated molecular pattern; PYD, pyrin domain; PRR, pattern recognition receptor; RIG-I, retinoic acid-inducible gene I; RIPK, receptor-interacting serine/threonine-protein kinase; TRAF, TNF receptor associated factor; WHD, winged helix domain

■ REFERENCES

(1) Pothlichet, J., and Quintana-Murci, L. (2013) The Genetics of Innate Immunity Sensors and Human Disease. *Int. Rev. Immunol. 32*, 157−208.

(2) Netea, M. G., van de Veerdonk, F. L., and van der Meer, J. W. M. (2012) Primary immunodeficiencies of pattern recognition receptors. *J. Int. Med. 272*, 517−527.

(3) Kawai, T., and Akira, S. (2011) Toll-like Receptors and Their Crosstalk with Other Innate Receptors in Infection and Immunity. *Immunity 34*, 637−650.

(4) Hu, Z., Yan, C., Liu, P., Huang, Z., Ma, R., Zhang, C., Wang, R., Zhang, Y., Martinon, F., Miao, D., Deng, H., Wang, J., Chang, J., and Chai, J. (2013) Crystal Structure of NLRC4 Reveals Its Autoinhibition Mechanism. *Science 341*, 172−175.

(5) Proell, M., Riedl, S. J., Fritz, J. H., Rojas, A. M., and Schwarzenbacher, R. (2008) The Nod-Like Receptor (NLR) Family: A Tale of Similarities and Differences. *PLoS One 3*, No. e2119.

(6) Franchi, L., Amer, A., Body-Malapel, M., Kanneganti, T.-D., Ozören, N., Jagirdar, R., Inohara, N., Vandenabeele, P., Bertin, J., Coyle, A., Grant, E. P., and Núñez, G. (2006) Cytosolic flagellin requires Ipaf for activation of caspase-1 and interleukin 1beta in salmonella-infected macrophages. *Nat. Immunol. 7*, 576−582.

(7) Manon, F., Favier, A., Núñez, G., Simorre, J.-P., and Cusack, S. (2007) Solution structure of NOD1 CARD and mutational analysis of

its interaction with the CARD of downstream kinase RICK. *J. Mol. Biol. 365*, 160−174.
(8) Park, J.-H., Kim, Y.-G., McDonald, C., Kanneganti, T.-D., Hasegawa, M., Body-Malapel, M., Inohara, N., and Núñez, G. (2007) RICK/RIP2 mediates innate immune responses induced through Nod1 and Nod2 but not TLRs. *J. Immunol. 178*, 2380−2386.
(9) Nembrini, C., Kisielow, J., Shamshiev, A. T., Tortola, L., Coyle, A. J., Kopf, M., and Marsland, B. J. (2009) The Kinase Activity of Rip2 Determines Its Stability and Consequently Nod1- and Nod2-mediated Immune Responses. *J. Biol. Chem. 284*, 19183−19188.
(10) Schneider, M., Zimmermann, A. G., Roberts, R. A., Zhang, L., Swanson, K. V., Wen, H., Davis, B. K., Allen, I. C., Holl, E. K., Ye, Z., Rahman, A. H., Conti, B. J., Eitas, T. K., Koller, B. H., and Ting, J. P.-Y. (2012) The innate immune sensor NLRC3 attenuates Toll-like receptor signaling via modification of the signaling adaptor TRAF6 and transcription factor NF-κB. *Nat. Immunol. 13*, 823−831.
(11) Meissner, T. B., Liu, Y.-J., Lee, K.-H., Li, A., Biswas, A., van Eggermond, M. C. J. A., van den Elsen, P. J., and Kobayashi, K. S. (2012) NLRC5 cooperates with the RFX transcription factor complex to induce MHC class I gene expression. *J. Immunol. 188*, 4951−4958.
(12) Staehli, F., Ludigs, K., Heinz, L. X., Seguín-Estévez, Q., Ferrero, I., Braun, M., Schroder, K., Rebsamen, M., Tardivel, A., Mattmann, C., MacDonald, H. R., Romero, P., Reith, W., Guarda, G., and Tschopp, J. (2012) NLRC5 deficiency selectively impairs MHC class I- dependent lymphocyte killing by cytotoxic T cells. *J. Immunol. 188*, 3820−3828.
(13) Cui, J., Zhu, L., Xia, X., Wang, H. Y., Legras, X., Hong, J., Ji, J., Shen, P., Zheng, S., Chen, Z. J., and Wang, R.-F. (2010) NLRC5 negatively regulates the NF-kappaB and type I interferon signaling pathways. *Cell 141*, 483−496.
(14) Davis, B. K., Roberts, R. A., Huang, M. T., Willingham, S. B., Conti, B. J., Brickey, W. J., Barker, B. R., Kwan, M., Taxman, D. J., Accavitti-Loper, M.-A., Duncan, J. A., and Ting, J. P.-Y. (2011) Cutting edge: NLRC5-dependent activation of the inflammasome. *J. Immunol. 186*, 1333−1337.
(15) Biswas, A., Meissner, T. B., Kawai, T., and Kobayashi, K. S. (2012) Cutting Edge: Impaired MHC Class I Expression in Mice Deficient for Nlrc5/Class I Transactivator. *J. Immunol. 189*, 516−520.
(16) Kumar, H., Pandey, S., Zou, J., Kumagai, Y., Takahashi, K., Akira, S., and Kawai, T. (2011) NLRC5 deficiency does not influence cytokine induction by virus and bacteria infections. *J. Immunol. 186*, 994−1000.
(17) Kobayashi, K. S., and van den Elsen, P. J. (2012) NLRC5: A key regulator of MHC class I-dependent immune responses. *Nat. Rev. Immunol. 12*, 813−820.
(18) Lamkanfi, M., and Kanneganti, T.-D. (2012) Regulation of immune pathways by the NOD-like receptor NLRC5. *Immunobiology. 217*, 13−16.
(19) Kersse, K., Verspurten, J., Vanden Berghe, T., and Vandenabeele, P. (2011) The death-fold superfamily of homotypic interaction motifs. *Trends Biochem. Sci. 36*, 541−552.
(20) Geertsma, E. R., and Dutzler, R. (2011) A versatile and efficient high-throughput cloning tool for structural biology. *Biochemistry 50*, 3272−3278.
(21) Keller, R. (2004) *The Computer Aided Resonance Assignment*, Cantina Verlag, Goldau, Switzerland.
(22) Grzesiek, S., and Bax, A. (1992) Correlating backbone amide and side chain resonances in larger proteins by multiple relayed triple resonance NMR. *J. Am. Chem. Soc. 114*, 6291−6293.
(23) Wittekind, M., and Mueller, L. (1993) HNCACB, a High-Sensitivity 3D NMR Experiment to Correlate Amide-Proton and Nitrogen Resonances with the Alpha- and Beta-Carbon Resonances in Proteins. *J. Magn. Reson. B 101*, 201−205.
(24) Kay, L. E., Ikura, M., Tschudin, R., and Bax, A. (1990) Three-dimensional triple-resonance NMR Spectroscopy of isotopically enriched proteins. *J. Magn. Reson. 89*, 496−514.
(25) Clubb, R. T., Thanabal, V., and Wagner, G. (1992) A constant-time three-dimensional triple-resonance pulse scheme to correlate intraresidue ^{1}HN, ^{15}N, and ^{13}Cα chemical shifts in ^{15}N,^{13}C-labelled proteins. *J. Magn. Reson. 1969* (97), 213−217.
(26) Bax, A., Clore, G. M., and Gronenborn, A. M. (1990) ^{1}H,^{1}H correlation via isotropic mixing of ^{13}C magnetization, a new three-dimensional approach for assigning ^{1}H and ^{13}C spectra of ^{13}C-enriched proteins. *J. Magn. Reson. 1969* (88), 425−431.
(27) Olejniczak, E. T., Xu, R. X., and Fesik, S. W. (1992) A 4D HCCH-TOCSY experiment for assigning the side chain ^{1}H and ^{13}C resonances of proteins. *J. Biomol. NMR 2*, 655−659.
(28) Yamazaki, T., Forman-Kay, J. D., and Kay, L. E. (1993) Two-dimensional NMR experiments for correlating ^{13}Cβ and ^{1}Hδ/ε chemical shifts of aromatic residues in ^{13}C-labeled proteins via scalar couplings. *J. Am. Chem. Soc. 115*, 11054−11055.
(29) Zerbe, O., Szyperski, T., Ottiger, M., and Wüthrich, K. (1996) Three-dimensional ^{1}H-TOCSY-relayed ct-[^{13}C, ^{1}H]-HMQC for aromatic spin system identification in uniformly ^{13}C-labeled proteins. *J. Biomol. NMR 7*, 99−106.
(30) Cornilescu, G., Delaglio, F., and Bax, A. (1999) Protein backbone angle restraints from searching a database for chemical shift and sequence homology. *J. Biomol. NMR 13*, 289−302.
(31) Herrmann, T., Güntert, P., and Wüthrich, K. (2002) Protein NMR structure determination with automated NOE assignment using the new software CANDID and the torsion angle dynamics algorithm DYANA. *J. Mol. Biol. 319*, 209−227.
(32) Herrmann, T., Güntert, P., and Wüthrich, K. (2002) Protein NMR structure determination with automated NOE-identification in the NOESY spectra using the new software ATNOS. *J. Biomol. NMR 24*, 171−189.
(33) Güntert, P. (2004) Automated NMR structure calculation with CYANA. *Methods Mol. Biol. 278*, 353−378.
(34) Brooks, B. R., Bruccoleri, R. E., Olafson, B. D., States, D. J., Swaminathan, S., and Karplus, M. (1983) CHARMM: A program for macromolecular energy, minimization, and dynamics calculations. *J. Comput. Chem. 4*, 187−217.
(35) Noggle, J. H., and Schirmer, R. E. (1971) *The Nuclear Overhauser Effect—Chemical Applications*, Academic Press, New York−London.
(36) Meiboom, S., and Gill, D. (1958) Modified Spin-Echo Method for Measuring Nuclear Relaxation Times. *Rev. Sci. Instrum. 29*, 688.
(37) Vold, R. L. (1968) Measurement of Spin Relaxation in Complex Systems. *J. Chem. Phys. 48*, 3831.
(38) Tollinger, M., Skrynnikov, N. R., Mulder, F. A., Forman-Kay, J. D., and Kay, L. E. (2001) Slow dynamics in folded and unfolded states of an SH3 domain. *J. Am. Chem. Soc. 123*, 11341−11352.
(39) Lipari, G., and Szabo, A. (1982) Model-free approach to the interpretation of nuclear magnetic resonance relaxation in macromolecules. 1. Theory and range of validity. *J. Am. Chem. Soc. 104*, 4546−4559.
(40) Lipari, G., and Szabo, A. (1982) Model-free approach to the interpretation of nuclear magnetic resonance relaxation in macromolecules. 2. Analysis of experimental results. *J. Am. Chem. Soc. 104*, 4559−4570.
(41) Fushman, D., Cahill, S., and Cowburn, D. (1997) The main-chain dynamics of the dynamin pleckstrin homology (PH) domain in solution: analysis of ^{15}N relaxation with monomer/dimer equilibration. *J. Mol. Biol. 266*, 173−194.
(42) Hall, J. B., and Fushman, D. (2003) Characterization of the overall and local dynamics of a protein with intermediate rotational anisotropy: Differentiating between conformational exchange and anisotropic diffusion in the B3 domain of protein G. *J. Biomol. NMR 27*, 261−275.
(43) Hall, J. B., and Fushman, D. (2006) Variability of the ^{15}N chemical shielding tensors in the B3 domain of protein G from ^{15}N relaxation measurements at several fields. Implications for backbone order parameters. *J. Am. Chem. Soc. 128*, 7855−7870.
(44) Walker, O., Varadan, R., and Fushman, D. (2004) Efficient and accurate determination of the overall rotational diffusion tensor of a molecule from ^{15}N relaxation data using computer program ROTDIF. *J. Magn. Reson. 168*, 336−345.
(45) Zuiderweg, E. R. P. (2002) Mapping Protein−Protein Interactions in Solution by NMR Spectroscopy. *Biochemistry 41*, 1−7.

(46) Aricescu, A. R., Lu, W., and Jones, E. Y. (2006) A time- and cost-efficient system for high-level protein production in mammalian cells. *Acta Crystallogr. D: Biol. Crystallogr. 62*, 1243−1250.
(47) Holm, L., and Rosenstrom, P. (2010) Dali server: Conservation mapping in 3D. *Nucleic Acids Res. 38*, W545−W549.
(48) Krissinel, E., and Henrick, K. (2004) Secondary-structure matching (SSM), a new tool for fast protein structure alignment in three dimensions. *Acta Crystallogr. D: Biol. Crystallogr. 60*, 2256−2268.
(49) Chou, J. J., Matsuo, H., Duan, H., and Wagner, G. (1998) Solution structure of the RAIDD CARD and model for CARD/CARD interaction in caspase-2 and caspase-9 recruitment. *Cell 94*, 171−180.
(50) Li, S., Yang, X., Shao, J., and Shen, Y. (2012) Structural Insights into the Assembly of CARMA1 and BCL10. *PloS One 7*, No. e42775.
(51) Srimathi, T., Robbins, S. L., Dubas, R. L., Hasegawa, M., Inohara, N., and Park, Y. C. (2008) Monomer/dimer transition of the caspase-recruitment domain of human Nod1. *Biochemistry 47*, 1319−1325.
(52) Humke, E. W., Shriver, S. K., Starovasnik, M. A., Fairbrother, W. J., and Dixit, V. M. (2000) ICEBERG: A novel inhibitor of interleukin-1β generation. *Cell 103*, 99−111.
(53) Hiller, S., Kohl, A., Fiorito, F., Herrmann, T., Wider, G., Tschopp, J., Grütter, M. G., and Wüthrich, K. (2003) NMR structure of the apoptosis- and inflammation-related NALP1 pyrin domain. *Structure 1993* (11), 1199−1205.
(54) Daragan, V. A., and Mayo, K. H. (1997) Motional model analyses of protein and peptide dynamics using ^{13}C and ^{15}N NMR relaxation. *Prog. Nucl. Magn. Reson. Spectrosc. 31*, 63−105.
(55) Ferrage, F., Dutta, K., Nistal-Villán, E., Patel, J. R., Sánchez-Aparicio, M. T., De Ioannes, P., Buku, A., Aseguinolaza, G. G., García-Sastre, A., and Aggarwal, A. K. (2012) Structure and dynamics of the second CARD of human RIG-I provide mechanistic insights into regulation of RIG-I activation. *Structure 1993* (20), 2048−2061.
(56) Qin, H., Srinivasula, S. M., Wu, G., Fernandes-Alnemri, T., Alnemri, E. S., and Shi, Y. (1999) Structural basis of procaspase-9 recruitment by the apoptotic protease-activating factor 1. *Nature 399*, 549−557.
(57) Kersse, K., Lamkanfi, M., Bertrand, M. J. M., Vanden Berghe, T., and Vandenabeele, P. (2011) Interaction patches of procaspase-1 caspase recruitment domains (CARDs) are differently involved in procaspase-1 activation and receptor-interacting protein 2 (RIP2)-dependent nuclear factor κB signaling. *J. Biol. Chem. 286*, 35874−35882.
(58) Kaczmarek, A., Vandenabeele, P., and Krysko, D. V. (2013) Necroptosis: The release of damage-associated molecular patterns and its physiological relevance. *Immunity 38*, 209−223.
(59) Fink, S. L., and Cookson, B. T. (2005) Apoptosis, Pyroptosis, and Necrosis: Mechanistic Description of Dead and Dying Eukaryotic Cells. *Infect. Immun. 73*, 1907−1916.
(60) Kuenzel, S., Till, A., Winkler, M., Häsler, R., Lipinski, S., Jung, S., Grötzinger, J., Fickenscher, H., Schreiber, S., and Rosenstiel, P. (2010) The nucleotide-binding oligomerization domain-like receptor NLRC5 is involved in IFN-dependent antiviral immune responses. *J. Immunol. 1950* (184), 1990−2000.
(61) Gack, M. U., Shin, Y. C., Joo, C.-H., Urano, T., Liang, C., Sun, L., Takeuchi, O., Akira, S., Chen, Z., Inoue, S., and Jung, J. U. (2007) TRIM25 RING-finger E3 ubiquitin ligase is essential for RIG-I-mediated antiviral activity. *Nature 446*, 916−920.
(62) Comeau, S. R., Gatchell, D. W., Vajda, S., and Camacho, C. J. (2003) ClusPro: An automated docking and discrimination method for the prediction of protein complexes. *Bioinformatics 20*, 45−50.